CrossMark

Green synthesis of α-Fe$_2$O$_3$/BiPO$_4$ composite and its biopolymeric beads for enhanced photocatalytic application

M. Nithya[1] · Keerthi Praveen[1] · S. Saral sessal[1] · U. Sathya[1] · N. Balasubramanian[2] · A. Pandurangan[1]

Abstract

This study reports a green and facile hydrothermal method to synthesis α-Fe$_2$O$_3$/BiPO$_4$ composite and was used for photocatalytic application under visible light irradiation. The synthesized samples were characterized by X-ray diffraction (XRD), scanning electron microscopy (SEM), transmission electron microscopy (TEM), UV–Vis diffuse reflectance spectrum (UV–Vis DRS), Fourier transform infrared (FT-IR) spectrum, X-ray photoelectron spectroscopy (XPS), Brunauer–Emmet–Teller (BET) analysis and Photoluminescence (PL), which confirmed the formation of the composite. XRD analysis indicated that all the prepared samples present in pure hexagonal structure without Fe$_2$O$_3$ phases. The photocatalytic studies on methylene blue (MB) and ciprofloxacin (CIP) were evaluated under visible light irradiation and the α-Fe$_2$O$_3$/BiPO$_4$ composite exhibited superior photocatalytic activity compared to the BiPO$_4$. The results of PL studies substantiated that the enhancement of photocatalytic activity could be mainly attributed to the interaction of α-Fe$_2$O$_3$ and BiPO$_4$ in the composite during photocatalysis which effectively improve electron–hole separation. The recyclability experiment corroborated the stability of α-Fe$_2$O$_3$/BiPO$_4$ composite. Finally, the composite was converted into beads using calcium alginate, a non toxic biopolymer for easy separation of the catalyst from the reaction medium, which also showed equally good results.

1 Introduction

Presently, the major quandary in the world is depletion and contamination of our limited water resources due to pollution and hence its consequences. Due to rapid industrialization and urbanization, the aquatic ecosystem is getting largely affected by toxic chemicals, dyes, pesticides and pharmaceutical wastages. The toxic and incalcitrant organic dyes released from textile industries into water bodies turn into severe crisis in environmental concern [1, 2]. The highly stable chemical structures of synthetic dyes cannot be simply degraded by conventional treatment methods such as adsorption, chemical coagulation, extraction and expensive membrane separation technologies, where the dyes are separated from the wastewater and not degraded. In recent years, semiconductor based photocatalysis is regarded as the most promising sustainable green chemical technology for water purification. It offers an easy way to degrade organic pollutants by converting solar energy into chemical energy [3–5].

Among the various semiconductor oxide photocatalysts, TiO$_2$ is the widely used catalyst for environmental applications due to its interesting optical and electrical properties, low cost, non toxicity and ease of availability. However, due to wide band gap energy of 3.2 eV, the main drawback of TiO$_2$ is that it is only active under UV radiation which corresponds to only 4% of the solar energy. The rapid recombination of electron–hole pairs also causes high operation cost [6–8]. The photocatalytic activity of TiO$_2$ is not prominent enough to meet the common and economical needs of industrial applications. Therefore, many researchers have shifted their focus on to finding a stable visible light driven photocatalyst to utilize solar energy at the maximum.

Recently, Bi(III) based semiconductor photocatalyst is concerned as a enhanced novel photocatalyst because of its good stability, non toxicity, cost effectiveness and improved photocatalytic activity in degrading organic pollutants. BiPO$_4$, a novel n-type non-metal oxyacid photocatalytic material, exhibits superior photocatalytic performance and it is found that the activity of BiPO$_4$ is twice that of TiO$_2$ for the degradation of methylene blue (MB) due to the inductive effect of phosphate group (PO$_4^{3-}$) [9]. But the photocatalytic

✉ Keerthi Praveen
dr.keerthi1012@gmail.com

1 Department of Chemistry, CEG campus, Anna University, Chennai 600025, India

2 Department of Chemical Engineering, A.C. Tech. Campus, Anna University, Chennai 600025, India

activity of $BiPO_4$ is also not enough to quench the need of the industries due to the rapid recombination of photogenerated electrons and holes and the wide band gap of $BiPO_4$ (3.85 eV) which limits its photocatalytic activity to the UV region [10, 11].

Many efforts have been taken to revise the properties of $BiPO_4$ to magnify its activity using energy of visible-light. Coupling two semiconductors to form a composite catalyst is considered as a competent approach towards harnessing the visible light and improving the separation efficiency of photogenerated charge carriers and hence augmenting the photocatalytic activity and stability [12, 13]. Fabrication of $Ag_3PO_4/BiPO_4$, $BiPO_4/BiOCl$ heterojunction shows greater photocatalytic ability under visible-light irradiation [14, 15]. $BiPO_4/Bi_2S_3$ heterojunction has also showed superior photocatalytic activity for the degradation of methylene blue (MB) under visible-light [16]. Hence, coupling of $BiPO_4$ with other semiconductors is still a more reached out research for improving light absorption in the visible spectrum and hence effectively restraining the recombination of photogenerated electron–hole pairs.

α-Fe_2O_3, a n-type semiconductor with narrow band gap of 2.2 eV [17], has been widely used for photocatalytic applications because of its properties which includes absorption in the visible range of the solar spectrum, high stability, low cost and its ease of availability. The distinct properties of α-Fe_2O_3, exhibits high separation capability and transport of photo carriers, because of its higher conduction band position and stronger reductive power [17–21]. Recently, the hierarchically structured α-Fe_2O_3/Bi_2WO_6 was reported which exhibits much enhanced photocatalytic activity in degradation of acid red G dye and Rhodamine-B (RhB) dye under visible-light irradiation [22]. $Fe_2O_3/BiOCl$ p–n heterojunctions was synthesized with high photocatalytic activity for the degradation of mixture of dyes under visible light irradiation [23]. Therefore, the combining of α-Fe_2O_3 and another semiconductor with suitable bandgap is a promising strategy to enhance the photocatalytic performance.

Hence it is suggested that α-Fe_2O_3 is suitable to employ a host/guest n/n junction with $BiPO_4$. The host material of $BiPO_4$ has a larger band gap than α-Fe_2O_3, and the conduction band of $BiPO_4$ is lower in energy than that of α-Fe_2O_3, allowing efficient electron transport across interface. To the best of our knowledge, a novel α-Fe_2O_3/$BiPO_4$ composite has been synthesized through simple hydrothermal method. The photocatalytic efficiency of α-Fe_2O_3/$BiPO_4$ composite has been evaluated by the degradation of methylene blue (MB) and ciprofloxacin (CIP) under visible light. The elaborate mechanism of enhanced photocatalytic activity of the composite is also proposed.

The industrial application of these photocatalysts demands easy separation and recovery of micro and nano-sized particles from the wastewater which are usually quite difficult and unpractical and hence requires additional separation units when it is applied in large scale reactors. A humble attempt has been made to convert the photocatalyst into spherical beads using alginate biopolymer owing to its biocompatibility, economical and toxicity aspect [24–31]. The present work elaborately discuss on the characterization and activity of the composite photocatalyst and photocatalytic bead towards MB degradation.

2 Materials and methods

Bismuth nitrate pentahydrate ($Bi(NO_3)_3 \cdot 5H_2O$), sodium phosphate ($Na_3PO_4 \cdot 12H_2O$), $Fe(NO_3)_3 \cdot 9H_2O$, sodium hydroxide (NaOH) and absolute ethanol were of analytical grade and were used without further purification. Distilled water was used throughout the whole experiment.

2.1 Synthesis of $BiPO_4$ nanorods

$BiPO_4$ was synthesized by using hydrothermal method. In the experimental process, 3 mmol of $Bi(NO_3)_3 \cdot 5H_2O$ (1.4552 g) and 3 mmol of $Na_3PO_4 \cdot 12H_2O$ (1.1403 g) were dissolved in 30 mL of distilled water separately under stirring for one hour. After vigorous stirring, $Na_3PO_4 \cdot 12H_2O$ solution was dropped into the former solution. White homogeneously suspended solution formed, indicates the formation of bismuth phosphate. The suspension was transferred into a 50 mL Teflon-lined stainless steel autoclave and heated in muffle furnace at 160 °C for 15 h and the solution was naturally cooled to room temperature. The obtained product was collected by centrifugation and washed with distilled water and ethanol, dried in oven at 60 °C overnight.

2.2 Synthesis of α-Fe_2O_3/$BiPO_4$ composite

The α-Fe_2O_3/$BiPO_4$ composites were also synthesized by hydrothermal method. 1 mmol of $BiPO_4$, 2 mmol NaOH and different amount of $Fe(NO_3)_3 \cdot 9H_2O$ (0.1, 0.2 and 0.3 mmol) were added into the beaker containing 80 mL of distilled water under constant stirring. The solution then was transferred into Teflon lined stainless steel autoclave of 100 mL capacity and heated at 160 °C for 15 h. The resultant products were separated through centrifugation and washed three times with distilled water and ethanol respectively. Finally, the products were dried in oven at 60 °C for overnight.

2.3 Preparation of α-Fe_2O_3/$BiPO_4$ alginate beads

Sodium alginate powder (1 g) was weighed and dissolved into 25 mL of distilled water with magnetic stirring for a period of 2 h to give a homogenous viscous solution. Separately 0.5 g of α-Fe_2O_3/$BiPO_4$ composite was sonicated for

30 min. This solution was then added to the alginate solution and stirred for 30 min. Alginate beads were formed on drop wise addition of the above mixture of viscous solution into the 2% CaCl$_2$ solution using a syringe. The beads were left in the 2% CaCl$_2$ solution for 24 h to obtain stable gel beads. The beads were washed several times with distilled water and stored in distilled water for further use. The beads turned red brown due to entrapment of α-Fe$_2$O$_3$/BiPO$_4$ composite by the alginate polymer and the ozone treated beads are shown in the Fig. 1.

2.4 Characterization

The surface morphology and composition of the samples were characterized by scanning electron microscopy (SEM, VEGA 3 TESCAN), transmission electron microscopy (TEM, JEOL 3010) and energy dispersive X-ray spectroscopy (EDS, Hitachi) respectively. The structure and crystallinity of the as-prepared samples were characterized by powder X-ray diffraction (XRD) analysis using XPERT-PRO diffractometer with Cu Kα radiation (I = 30 mA, V = 40 kV) and the scanning range was 10°–80°. UV–Vis diffuse reflectance spectra (DRS) measurements were done using a UV–Visible spectrophotometer (PG Instruments-T90). X-Ray photoelectron spectroscopy (XPS) was carried out using a PHI 5000 VERSAPROBE II SCANNING ESCA MICROPROBE system with a monochromatic Al Kα source. The chemical bonds of the composites were detected by the Fourier transform infrared (FT-IR) spectroscopy (ABB MB 3000). The Brunauer–Emmett–Teller (BET) specific surface areas of the samples were evaluated on the basis of nitrogen adsorption isotherms measured at 77 K using a Quantachrome Instrument version 3.0. The sample was degassed at 150 °C before nitrogen adsorption measurements. The BET surface area was determined using the adsorption–desorption data in the relative pressure (p/p$_0$) range of 0.015–0.951. The UV–Vis absorption spectra were recorded using Elico SL-159 UV–Vis spectrophotometer. The photoluminescene (PL) measurements were carried out

on a JY Fluorolog-3-11 Spectrofluorometer with an excitation wavelength of 300 nm at room temperature.

2.5 Photocatalysis

The photocatalytic activity of the samples was evaluated by the degradation of MB and CIP aqueous solution under visible light irradiation. The experiments were performed at room temperature and 500W tungsten halogen lamp with a λ > 400 nm was used as the visible light source. 100 mg of the prepared catalyst was added into 100 mL MB or CIP aqueous solutions (10 mg/L). Prior to illumination, the suspensions were continuously stirred for 1 h in the dark to reach an adsorption–desorption equilibrium. A small amount of sample was collected at regular interval and centrifuged to remove the photocatalyst powders. The concentration of MB or CIP aqueous solution was analyzed using Elico SL159 UV–Vis spectrophotometer at maximum absorption (664 nm for MB and 276 nm for CIP). The chemical oxygen demand (COD) was determined by the potassium dichromate method. The stability of the α-Fe$_2$O$_3$/BiPO$_4$ composite catalyst and its alginate beads were evaluated by reusing the catalyst for four runs for the decomposition of methylene blue under the same conditions. After each run, the catalyst was separated by centrifugation procedure, washed with water and ethanol. The alginate beads were washed using water and ethanol but after second and third wash the beads started shrinking and disintegrating, therefore ozone treatment for the beads was adopted for 30 min, washed with distilled water and reused.

2.6 Photoelectrochemical measurements

Photocurrent measurement was performed with CHI608E electrochemical workstation in a standard three electrode configuration with a Pt wire as the counter electrode, Ag/AgCl electrode as a reference electrode and synthesized catalyst coated on FTO conducting glass as a working electrode. A 250W Xenon arc lamp served as a light source and

Fig. 1 Photographs of alginate beads at different stages

Alginate beads before reaction　　　**After reaction**　　　**After ozone treatment**
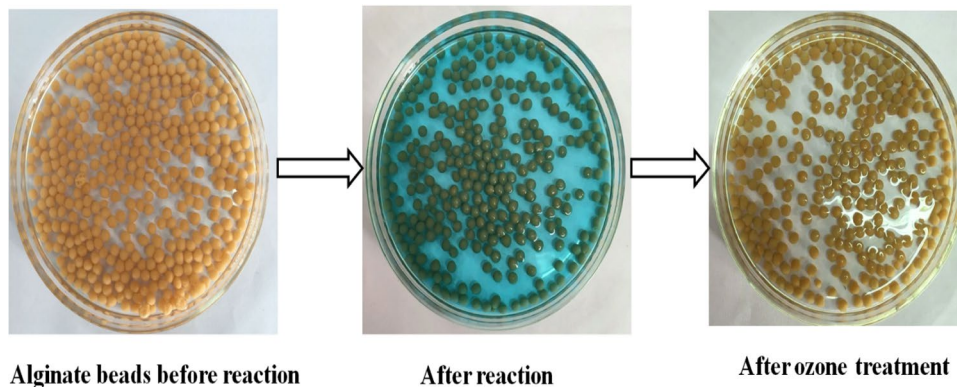
0.1 M Na_2SO_4 aqueous solution was used as the electrolyte. The working electrode was prepared as follows: the 50 mg of sample was mixed with 1 mL ethanol to make slurry and then ultrasonicated for 20 min. The turbid liquid was coated on to a FTO glass electrode and these electrodes were dried at 80 °C for 6 h.

2.7 Radical scavenger experiment

The main reactive species (radicals and holes) were detected through radical scavenging experiments in the photocatalytic process. The holes (h^+), hydroxyl radical (·OH) and superoxide radical (·O_2^-) are trapped by adding ammonium oxalate (AO), isoproapanol (IPA) and p-benzoquinone (p-BQ) respectively into the reaction solution, during the process of photocatalytic degradation of MB. Typically, 100 mg of catalyst and 10 mM of radical scavengers were added into 100 mL of 10 mg/L MB dye solution and the suspension was irradiated using the visible lamp. Finally, the C/C_0 of the dye can be calculated to determine the main active species.

3 Results and discussion

3.1 XRD analysis

The detailed information on the crystal structure and phase purity of the as prepared samples was obtained by the powder X-ray diffraction (XRD) measurement. Figure 2 displays the typical XRD patterns of the $BiPO_4$ and α-Fe_2O_3/$BiPO_4$ composites with different molar ratios. It can be found that all the diffraction peaks of $BiPO_4$ and the composites could be well indexed to the hexagonal $BiPO_4$ (JCPDS File No. 45-1370). The diffraction peaks of α-Fe_2O_3 were not observed in the 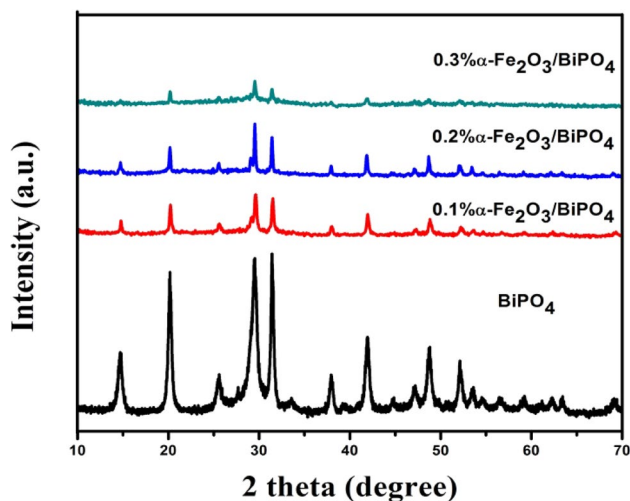XRD patterns of composites because its content in the composite is lower than the XRD limit of detection [32]. But the peak intensities decreased in composites due to small amount of α-Fe_2O_3. No other diffraction peaks were observed, indicating the high purity of the sample. Further the presence of α-Fe_2O_3 could be confirmed by EDX and XPS analysis.

3.2 FTIR analysis

The FTIR spectrum of $BiPO_4$, 0.1% α-Fe_2O_3/$BiPO_4$, 0.2% α-Fe_2O_3/$BiPO_4$ and 0.3% α-Fe_2O_3/$BiPO_4$ samples are shown in the Fig. 3. The spectrum displays the main absorption peak in the region of 3499 cm^{-1} assigned to the O–H stretching vibrations and a peak at 1605 cm^{-1} attributed to the bending vibrations of physically adsorbed water (O–H–O) existing on the catalyst surfaces. These bands are very essential for photocatalytic degradation process because they can react with the photoexcited holes on the catalyst surface and produce a hydroxyl radical which is useful to oxidize the organic pollutants. The peak at 1022 cm^{-1} corresponds to the ν_3 asymmetric stretching vibrations of the PO_4 groups [33]. The peaks observed at 594 and 535 cm^{-1} correspond to the (O–P–O) and ν_4 (PO_4) bending vibrations of PO_4 groups, respectively. A small band at 477 cm^{-1} is ascribed to Fe–O bond which is detected in all samples indicating the presence of ferric oxide in the composites.

3.3 Morphology and elemental composition analysis

The surface morphologies of the obtained $BiPO_4$, 0.1% α-Fe_2O_3/$BiPO_4$ composites and 0.1% α-Fe_2O_3/$BiPO_4$
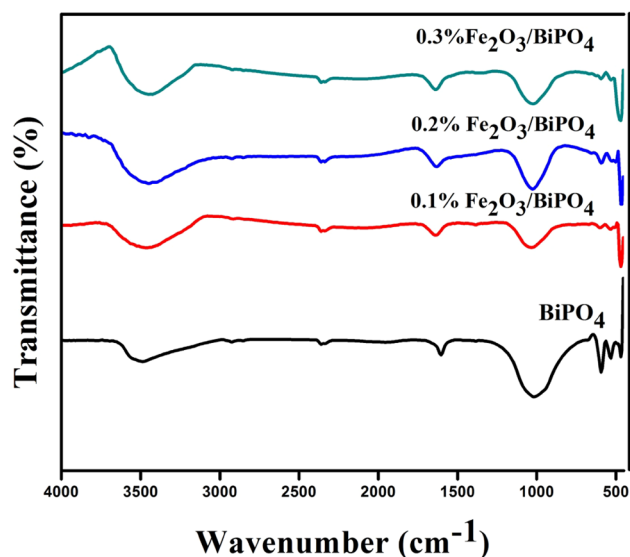
Fig. 2 XRD patterns of $BiPO_4$ and α-Fe_2O_3/$BiPO_4$ composites

Fig. 3 FTIR spectra of $BiPO_4$ and α-Fe_2O_3/$BiPO_4$ composites

alginate beads were characterized by SEM, as shown in Fig. 4a–d. The pure $BiPO_4$ consisted of irregular nanorods and composites consisted of irregular rods ($BiPO_4$) and spherical particles (Fe_2O_3), which was again confirmed by the TEM analysis (Fig. 4e). Surface and cross sectional images of 0.1% α-Fe_2O_3/$BiPO_4$ alginate beads shows the photocatalyst spread over the surface and inside the beads. Figure 4f shows the EDX analysis of the 0.1% α-Fe_2O_3/$BiPO_4$ composite. The existence of Fe_2O_3 and $BiPO_4$ in the composite has been proved by the peaks of Fe, Bi, P and O in EDX data. This confirms the presence of Fe_2O_3 in the final product.

3.4 XPS analysis

The elemental composition and the chemical states of the constituent elements of $BiPO_4$ and 0.1% α-Fe_2O_3/$BiPO_4$ composite were evaluated by using of XPS. Figure 5a shows the XPS full spectra of $BiPO_4$ and 0.1% α-Fe_2O_3/$BiPO_4$ composite and peaks show that the composite mostly contains Bi, P, O and Fe elements. The carbon element can be attributed to the adventitious hydrocarbon from XPS instrument itself. The corresponding XPS spectra of the above four elements in the $BiPO_4$ and 0.1% α-Fe_2O_3/$BiPO_4$ composite are presented in Fig. 5b–e. As shown in Fig. 5b, the peaks located at 159.2 and 164.5 eV are attributed to Bi 4f7/2 and Bi 4f5/2, respectively, indicating the existence of Bi^{3+} ions for $BiPO_4$. For composites these two peaks shifts to low binding energy by approximately 0.9 eV. The shifting of the binding energy indicates that electron transfer occurs from Fe_2O_3 to $BiPO_4$ [34]. It can be concluded that the strong coupling exists between $BiPO_4$ and Fe_2O_3 in the composite. The peak with binding energy of 530.6 eV (Fig. 5c) corresponds to the lattice oxygen in $BiPO_4$, but it shift to 529.7 eV for 0.1% α-Fe_2O_3/$BiPO_4$ composite. The XPS peak of P 2p can be observed at binding energy 132.8 eV for $BiPO_4$ and 132.4 eV for composite (Fig. 5d), indicating the existence of P in the composite. Figure 5e shows the XPS peaks of Fe 2p which was observed at 709.5 and 723.9 eV, and can be assigned to Fe 2p3/2 and Fe 2p1/2 peaks in α-Fe_2O_3 phase, respectively. The shake-up satellite at 717.6 eV was observed and it is the characteristic of Fe^{3+} in α-Fe_2O_3 [35, 36]. The XPS analysis result indicates the presence

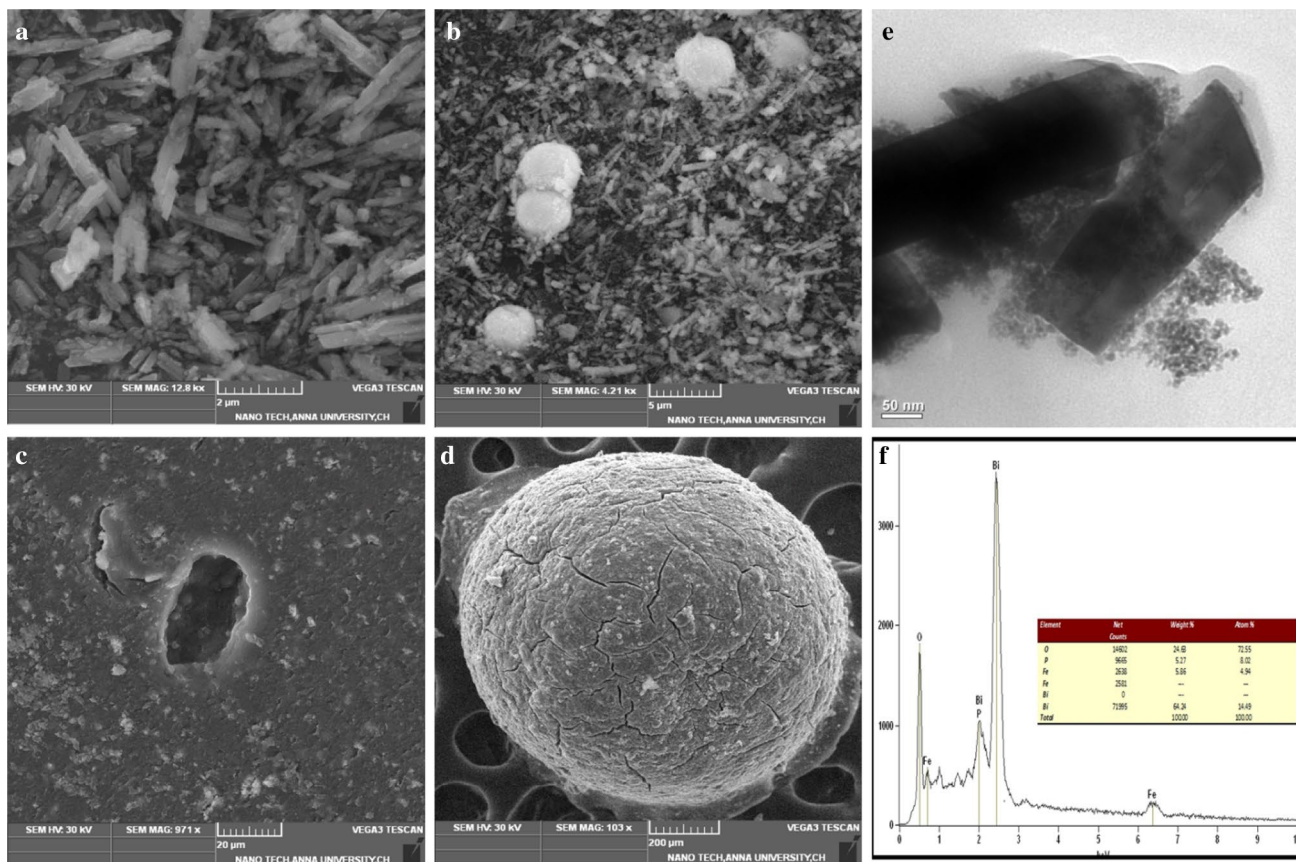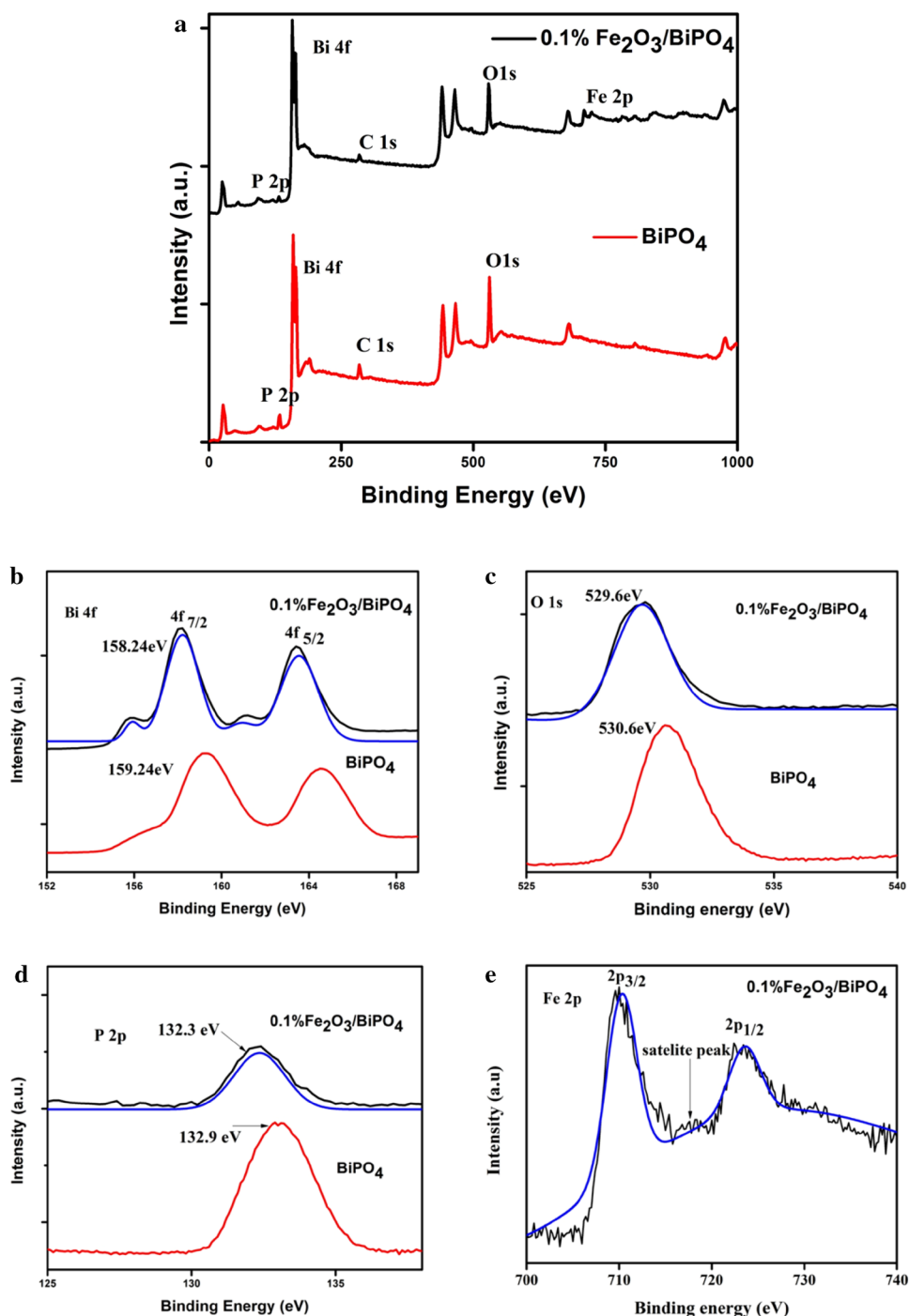**Fig. 4** SEM images of **a** $BiPO_4$, **b** 0.1% α-Fe_2O_3/$BiPO_4$, **c** beads cross section, **d** beads surface and **e** TEM image and **f** EDX spectra of 0.1% α-Fe_2O_3/$BiPO_4$

Fig. 5 a XPS full spectra of BiPO$_4$ and 0.1% α-Fe$_2$O$_3$/BiPO$_4$ composite, High resolution XPS spectra of **b** Bi 4f, **c** O 1s, **d** P 2p and **e** Fe 2p

of α-Fe$_2$O$_3$ in the composite and substantiates the electron transfer between BiPO$_4$ and Fe$_2$O$_3$.

3.5 BET analysis

The BET surface area of 0.1% α-Fe$_2$O$_3$/BiPO$_4$ was investigated using nitrogen adsorption–desorption experiment (Fig. 6). The N$_2$ adsorption–desorption isotherm is of type IV with a distinct hysteresis loop observed in

the range of 0.7–1.0 p/p$_0$. The composite exhibits high adsorption at relative pressures p/p$_0$ close to 1.0, signifying the formation of large mesopores and macropores (Pore volume 0.038 cc/g and pore diameter 3.661 nm). The 0.1% α-Fe$_2$O$_3$/BiPO$_4$ exhibits a higher surface area (14.178 m^2/g) than pure BiPO$_4$ (3 m^2/g) [9]. The higher surface area of the composite is yet another boon for the efficient photodegradation of organic pollutants [37, 38].
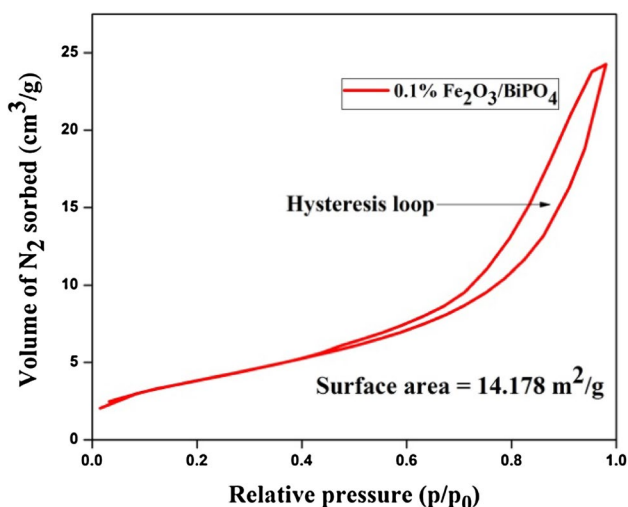
Fig. 6 N_2 adsorption/desorption curves at 77 K for 0.1% α-Fe_2O_3/ $BiPO_4$ composite

3.6 Optical properties

The diffuse reflectance spectra of $BiPO_4$ and 0.1% α-Fe_2O_3/ $BiPO_4$ composite is shown in Fig. 7. The absorption band edge of $BiPO_4$ is found to be about 332 nm and for 0.1% α-Fe_2O_3/ $BiPO_4$ composite is about 382 nm which indicates red shift compared with pure $BiPO_4$. The composite shows visible light absorption, which is due to the presence of Fe_2O_3. The band-gap of the samples are estimated using equation.
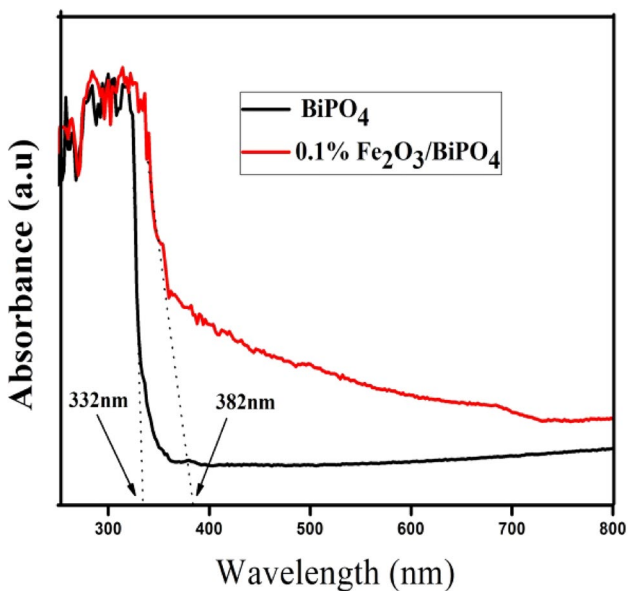
$$Eg = 1240/\lambda \tag{1}$$

where Eg is the bandgap, λ is the absorbance band edge in the UV–Vis DRS analysis. The band gap calculated from the above equation is 3.73 and 3.24 eV respectively for $BiPO_4$ and 0.1% α-Fe_2O_3/$BiPO_4$, which shows the reduction in the band gap due to the incorporation of Fe_2O_3 in the composites. The above results are ascribed to the chemical interaction between Fe_2O_3 and $BiPO_4$ in the composite, which has improved the separation and transfer of electron–hole pairs during photocatalysis.

3.7 Photoluminescence spectral analysis

Generally, photocatalytic reactions are more dependent on the rate of electron–hole recombination. The separation capacity of photogenerated electron and hole pairs can be studied by photoluminescence (PL) emission intensity. A weaker intensity of the emission peak in PL indicates lesser recombination rate of electron–hole pairs [39]. Hence, the PL spectra of $BiPO_4$ and 0.1% α-Fe_2O_3/ $BiPO_4$ composite were recorded at excitation wavelength of 300 nm in room temperature as shown in Fig. 8. The results show significant decrease in relative PL intensity of 0.1% α-Fe_2O_3/$BiPO_4$ compared to the $BiPO_4$ indicating that the recombination of photogenerated charge carriers was suppressed greatly through the α-Fe_2O_3/$BiPO_4$ composite formation. The PL results therefore confirm the importance of the composite in retarding electron–hole recombination and hence enhancing the photocatalytic performance.
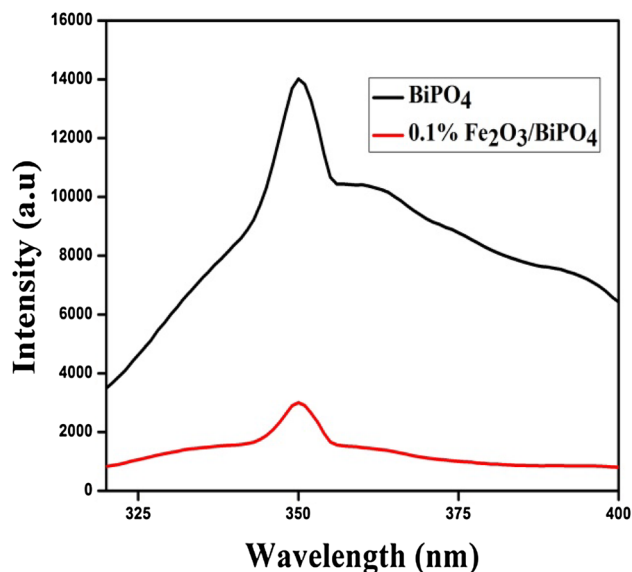

Fig. 7 UV–Visible diffuse reflectance spectra of $BiPO_4$ and 0.1% α-Fe_2O_3/$BiPO_4$ composite

Fig. 8 Photoluminescence spectra of $BiPO_4$ and 0.1% α-Fe_2O_3/$BiPO_4$ composite

3.8 Photocatalytic activity

The photocatalytic efficiency of $BiPO_4$ and the α-Fe_2O_3/$BiPO_4$ composites was evaluated by degradation of MB and CIP under visible light ($\lambda \geq 420$ nm) irradiation. Figure 9a–c showed the photocatalytic activities of the $BiPO_4$ and composites under visible light irradiation. The degradation efficiency of all catalysts was calculated using the following equation.

$$\text{Degradation \%} = \frac{C_0 - C_t}{C_0} \times 100 \qquad (2)$$

where C_t is the concentration of MB or CIP at time t and C_0 is the concentration of MB or CIP at adsorption equilibrium, before irradiation. Only 44% of MB was degraded after 180 min of irradiation with pure $BiPO_4$. All of the α-Fe_2O_3/$BiPO_4$ photocatalysts exhibited higher photocatalytic activity than the pure $BiPO_4$ under visible light, which is definitely due to the presence of Fe_2O_3 in the composites and its capability to absorb visible light. In particular, the 0.1% α-Fe_2O_3/$BiPO_4$ composites exhibit the highest photocatalytic activity for the degradation of MB which is 96% within 180 min. Further the photocatalytic degradation efficiencies of theα-Fe_2O_3/$BiPO_4$ decreased with the increase of α-Fe_2O_3, which may be due to the increased photogenerated electron–hole pair recombination of Fe_2O_3. Hence, it is clear that the optimum molar ratio of Fe_2O_3 to $BiPO_4$ is 0.1 mol% for the effective photocatalytic degradation of MB.

For further confirmation of the photocatalytic performance of the 0.1% α-Fe_2O_3/$BiPO_4$ composite, colorless pharmaceutical pollutant CIP was used to perform photocatalytic degradation experiment under visible light irradiation. Figure 9c shows the characteristic absorption peak of CIP at 276 nm, and the relative decrease in the intensity of the UV–Vis spectra over time, indicating the photocatalytic degradation (56%) of CIP. These results confirm that the degradation of the MB dye was associated to the photocatalytic activity of 0.1%α-Fe_2O_3/$BiPO_4$ rather than dye sensitization and that CIP could not sensitize photocatalysis under visible light irradiation [40].

The photocatalytic efficiency of the 0.1% α-Fe_2O_3/$BiPO_4$ incorporated alginate beads was also evaluated. The photocatalytic activity of the beads was then compared with the corresponding powder samples. This experiment were carried out for the bead sample containing the exact amount of composite as that of the powder sample, thus any difference in their catalytic or adsorption efficiency can be ascribed to the presence of the alginate in the case of beads. Figure 10a, b, shows the degradation efficiency of powder catalysts and beads. The adsorption capacity of beads is higher than the powder which can be attributed to the presence of alginate polymer. Alginate beads have been already proposed for the
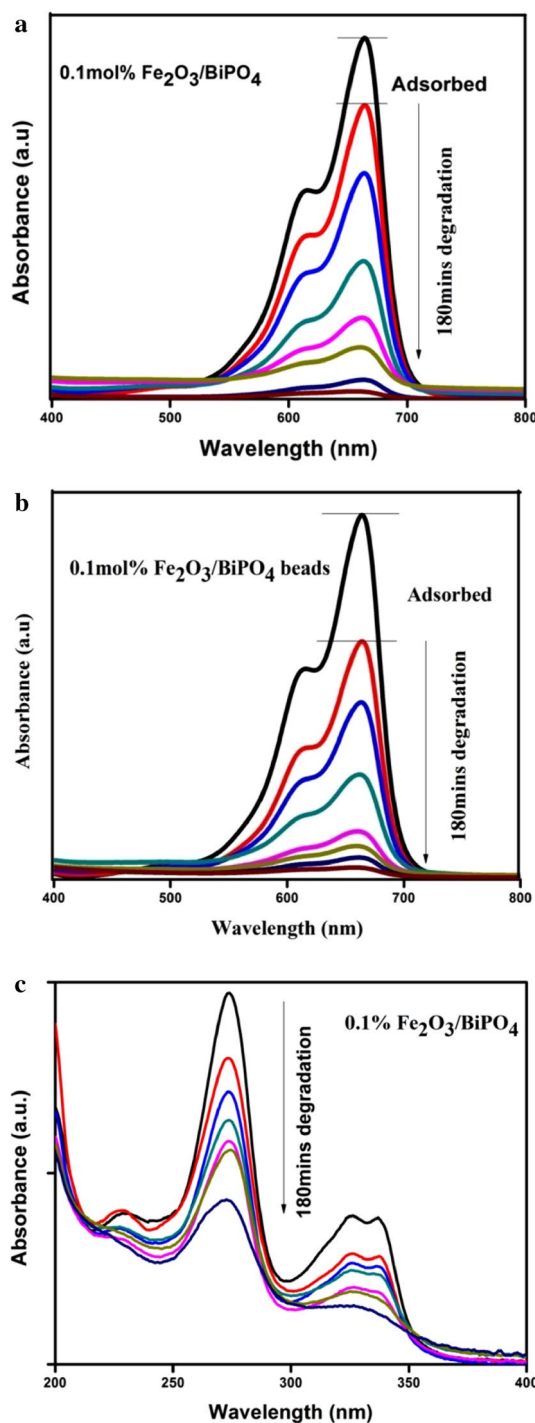

Fig. 9 UV–Vis absorbance of MB during photocatalytic degradation in the presence of **a** 0.1% α-Fe_2O_3/$BiPO_4$ composite **b** 0.1% α-Fe_2O_3/$BiPO_4$ alginate beads and CIP degradation in **c** 0.1% α-Fe_2O_3/$BiPO_4$ composite

efficient removal of several organic dyes [31]. The photocatalytic activity of the beads is slightly lower than that of the composite (Fig. 10a). The time required to degrade the same amount of MB solution is higher for the bead samples
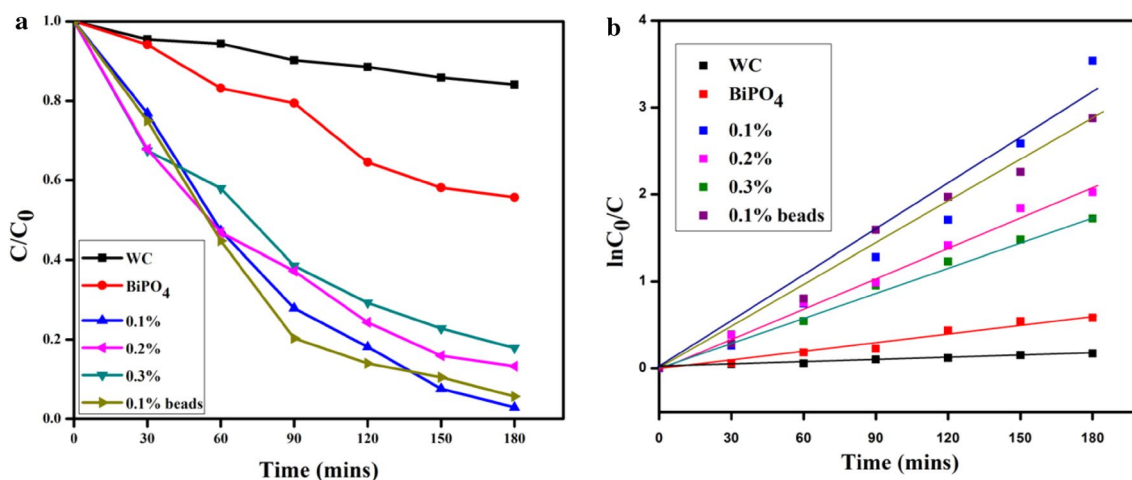
Fig. 10 Comparison of **a** photocatalytic degradation and **b** kinetics of MB for different photocatalytic systems as a function of irradiation time

due to the reduction of the surface area and saturation of the surface active sites. However the above limitations are compensated by the following advantages.

1. The beads can be easily recovered from the wastewater compared to the powder sample.
2. The same beads can be used for more cycles.

Furthermore to understand the reaction kinetics of the photocatalytic degradation of MB, the apparent rate constant k, was calculated from the following equation and this process followed with the first order reaction:

$$\ln \left(C_t / C_0 \right) = kt \tag{3}$$

where, C_0 and C_t are the concentrations of the MB solution at time 0 and t, respectively. The photocatalytic degradation rate constants (k) of $BiPO_4$ and α-Fe_2O_3/$BiPO_4$ composites are shown in Fig. 10b. The rate constant of pure $BiPO_4$ is due to dye sensitized reaction. The rate constant (k) of 0.1% α-Fe_2O_3/$BiPO_4$ photocatalyst was 0.0173 min^{-1}, which was six times higher than that of pure $BiPO_4$ (0.0031 min^{-1}). Among all the α-Fe_2O_3/BiPO4 composites, the 0.1% α-Fe_2O_3/$BiPO_4$ composite exhibits highest k value than that of other xFe_2O_3/$BiPO_4$ (x = 0.2, 0.3) and alginate beads photocatalyst, which are 0.0093, 0.0118 and 0.0150 min^{-1} respectively. These results indicate the combination of Fe_2O_3 to the $BiPO_4$ is enhancing the photocatalytic activity of $BiPO_4$ in the visible light region.

Testing the chemical stability and the recycling capability of photocatalyst is important for practical application. The reusability of 0.1% α-Fe_2O_3/$BiPO_4$ composite and its alginate beads were evaluated by recycling the photocatalytic degradation of MB experiments under same conditions. Figure 11a shows the photocatalytic efficiency of composites and its beads after four times of cycling test, indicating that

the sample possesses stability. In addition, the FT-IR pattern of 0.1% α-Fe_2O_3/$BiPO_4$ before and after photocatalytic reaction did not show any discrepancy and hence shows the stability of the structure (Fig. 11b). To further investigate the photocatalytic degradation efficiency of the composite, the removal of COD of MB was analyzed and the results are showed in Fig. 11c. The COD removal efficiency of the 0.1% composite is the higher compared to other composites. The removal of COD agrees well with the results of photocatalytic degradation. This results confirm the catalyst not only decolorize but also degrades the MB solution.

3.9 Possible mechanism for photocatalytic degradation of MB

To further investigate the photocatalytic mechanism, trapping experiments were carried out to determine the main reactive species involved in the photocatalytic process (Fig. 11d). When Ammonium oxalate was used (AO, hole sacavenger), no obvious change in photocatalytic performance could be observed, suggesting that photoexcited holes were not the major reactive species. The photocatalytic activity of 0.1%α-Fe_2O_3/$BiPO_4$ composite slightly decreased by the introduction of benzoquinone (BQ, $O_2^{\cdot -}$ radical scavenger), indicating that $O_2^{\cdot -}$ radical played a minor role in MB degradation. On the other hand, the degradation efficiency was significantly decreased by the addition of isopropanol (IPA) employed as a $\cdot$OH radical scavenger which suggested that the $\cdot$OH radical played a major role in MB degradation.

The photo-electrochemical measurement were used to investigate the charge separation efficiency of electrons and holes. To study the charge separation efficiency of the photocatalyts, the transient photocurrent responses were recorded for pure $BiPO_4$ and 0.1% α-Fe_2O_3/$BiPO_4$ composite
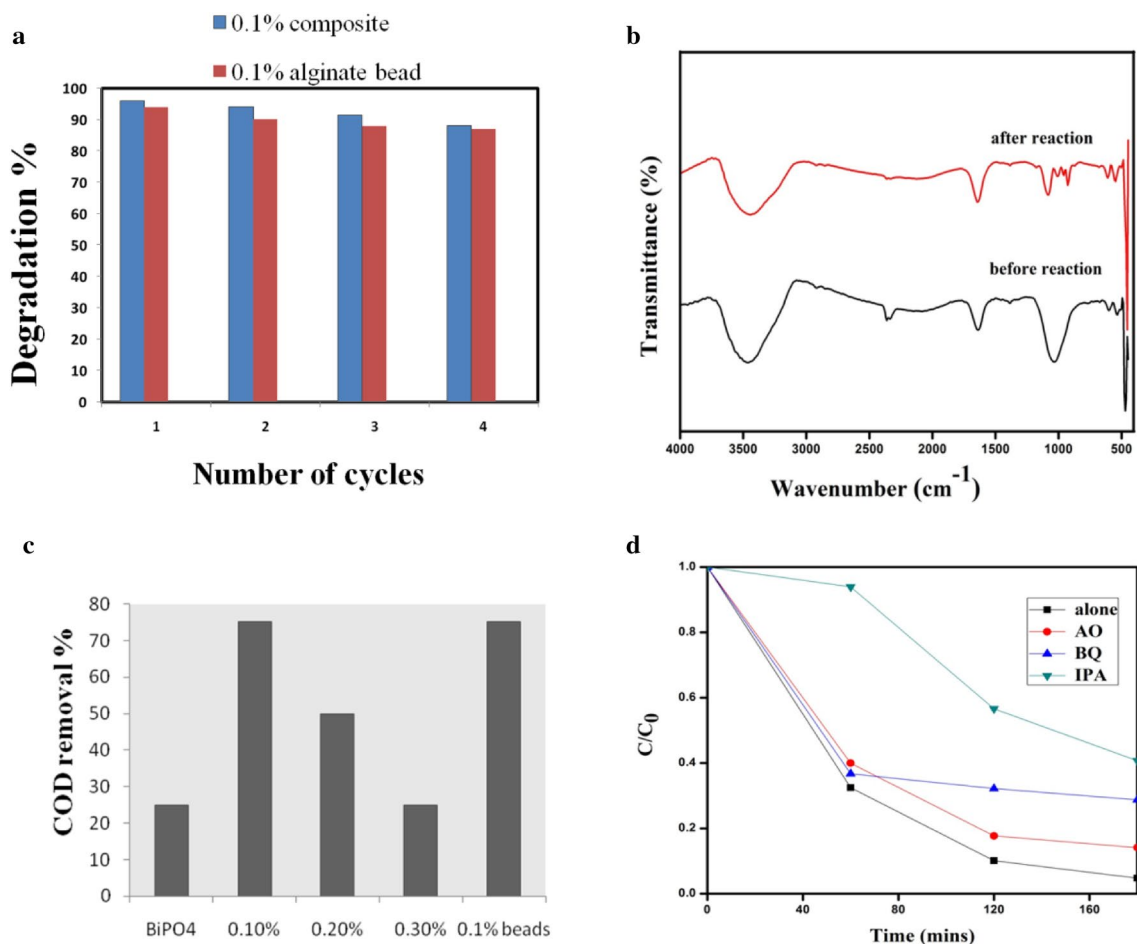
Fig. 11 **a** Recyclability test, **b** FTIR spectra, **c** COD Removal in MB degradation at 3 h and **d** Trapping experiments of active species over 0.1% α-Fe$_2$O$_3$/BiPO$_4$ sample

photocatalysts with typical two on–off cycles under visible-light irradiation and the obtained results are shows in the Fig. 12. The photostability of all the photocatalyst was also confirmed from a reproducible photocurrent response for few on–off cycles under visible-light irradiation. Figure 12 indicates that the photocurrent response of α-Fe$_2$O$_3$/BiPO$_4$ composite is higher than that of pure BiPO$_4$. This suggests that the α-Fe$_2$O$_3$/BiPO$_4$ composite is efficient in electron–hole separation than the bare BiPO$_4$.

From the above results possible mechanism has been proposed for the degradation of MB by α-Fe$_2$O$_3$/BiPO$_4$ photocatalyst. A schematic diagram for electron–hole separation and transportation between α-Fe$_2$O$_3$/BiPO$_4$ photocatalyst interface is shown in Fig. 13. Photocatalytic activity of α-Fe$_2$O$_3$/BiPO$_4$ composite is higher than that of BiPO$_4$. The energy match between two semiconductors is responsible for the efficient production and separation of the electron–hole pairs. The band gap of BiPO$_4$ and Fe$_2$O$_3$ is 3.85 and 2.2 eV [17] respectively. The wide bandgap of BiPO$_4$ inhibit the absorption of visible light, but Fe$_2$O$_3$ absorb visible light and produce electron and
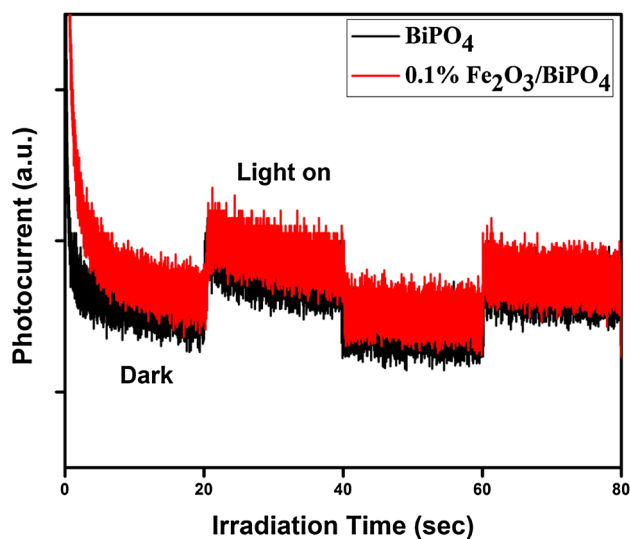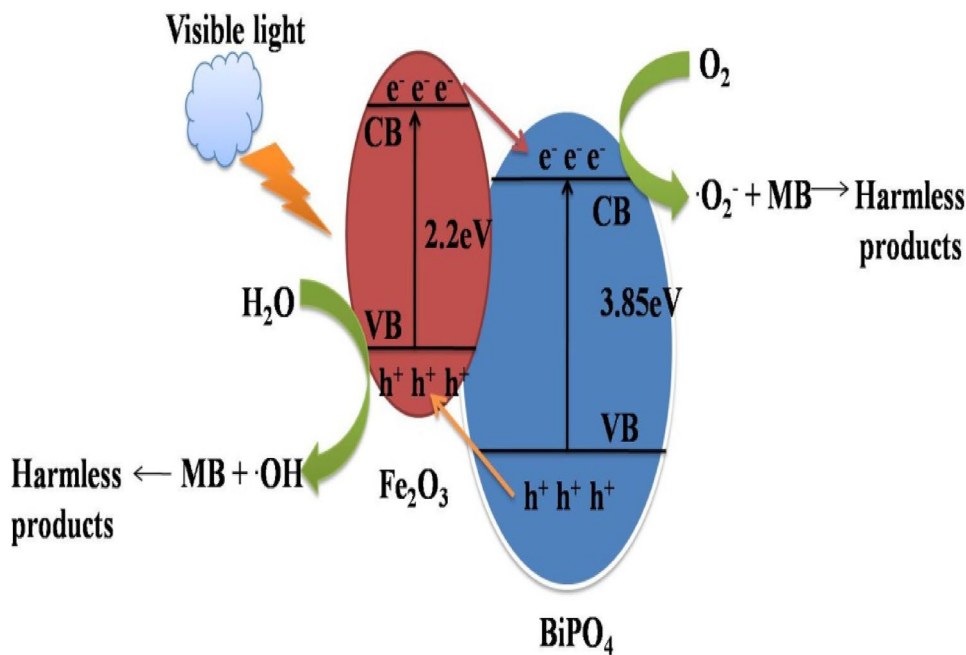

Fig. 12 Transient photocurrent density responses of BiPO$_4$ and 0.1% α-Fe$_2$O$_3$/BiPO$_4$ with light on/off cycles under visible light

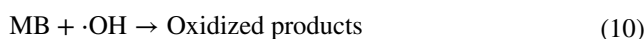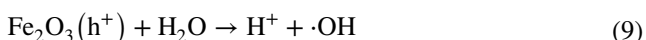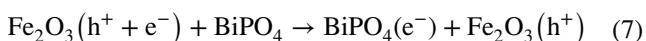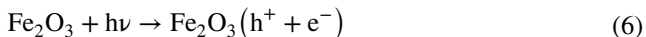**Fig. 13** The proposed mechanism and electron–hole pair separation of α-Fe$_2$O$_3$/BiPO$_4$ composites

hole pairs. The band edge positions of the conduction band (CB) and valence band (VB) of a semiconductor can be determined using the following equation.

$$E_{VB} = X - E^e + 0.5Eg \qquad (4)$$

$$E_{CB} = E_{VB} - E_g \qquad (5)$$

where E_{VB} is the valence band edge potential, E_{CB} is the conduction band edge potential, X is the electronegativity of the semiconductor, E^e is the energy of free electrons on the hydrogen scale ($E^e = 4.5$ eV) and Eg is the band gap energy of the semiconductor. From the calculation E_{VB} and E_{CB} value of BiPO$_4$ and Fe$_2$O$_3$ was found to be 3.25, − 0.48 and 1.38, − 0.82 eV respectively [9, 22]. The conduction band edge potential of Fe$_2$O$_3$ is more negative than that of BiPO$_4$ and valance band edge potential of BiPO$_4$ was more positive than that of Fe$_2$O$_3$. Thus the photogenerated electrons transfer happens from Fe$_2$O$_3$ to the CB of BiPO$_4$, while the holes are transferred to VB of Fe$_2$O$_3$. This process reduces the recombination rate of electron–hole pair and increases the charge separation, which leads to the more photocatalytic activity of α-Fe$_2$O$_3$/BiPO$_4$ composite.

The possible pathway for degradation of MB can be described as follows.

$$Fe_2O_3 + h\nu \rightarrow Fe_2O_3\left(h^+ + e^-\right) \qquad (6)$$

$$Fe_2O_3\left(h^+ + e^-\right) + BiPO_4 \rightarrow BiPO_4(e^-) + Fe_2O_3\left(h^+\right) \qquad (7)$$

$$BiPO_4(e^-) + O_2 \rightarrow \cdot O_2^- \qquad (8)$$

$$Fe_2O_3\left(h^+\right) + H_2O \rightarrow H^+ + \cdot OH \qquad (9)$$

$$MB + \cdot OH \rightarrow \text{Oxidized products} \qquad (10)$$

4 Conclusion

The α-Fe$_2$O$_3$/BiPO$_4$ composites were successfully synthesized by a facile hydrothermal method. Coupling of BiPO$_4$ with α-Fe$_2$O$_3$ promotes the visible light absorption and photocatalytic activity of BiPO$_4$ to a superior extent. The photocatalytic performance of bare BiPO$_4$ and α-Fe$_2$O$_3$/BiPO$_4$ composites were evaluated under visible light irradiation for the degradation of MB and CIP. The PL spectra confirm the enhanced photocatalytic activity of the composite resulting from the reduced recombination rate of electron–hole pair. The photocatalytic activity and stability of the composite was retained after four reaction cycles. Radical scavenging tests indicated that hydroxyl radicals are the main reactive species for the degradation of MB. The compact form of composite with an alginate biopolymer improves effortless separation of catalyst from the reaction medium and showed similar degradation results. Further the efficiency of the photocatalyst can be enhanced by increasing the surface area through conversion to nanocomposite, for which efforts are being taken by the authors. Therefore α-Fe$_2$O$_3$/BiPO$_4$ composite is one of the suitable photocatalysts in water remediation and composite beads can represent promising materials for developing a new generation of green-catalysts.

References

1. O. Shan, M.R. Karthikeyan, Reduction of textile dye by using heterogeneous photocatalysis. Am. J. Environ. Prot. **3**, 90–94 (2013)

2. L.L. Yuan, D.D. Huang, W.N. Guo, Q.X. Yang, J. Yu, TiO_2/montmorillonite nanocomposite for removal of organic pollutant. Appl. Clay Sci. **53**, 272–278 (2011)

3. H. Fan, Y. Li, B. Liu, Y. Lu, T. Xie, D. Wang, Photoinduced charge transfer properties and photocatalytic activity in Bi_2O_3/$BaTiO_3$ composite photocatalyst. ACS Appl. Mater. Interfaces **4**, 4853–4857 (2012)

4. H. Tong, S. Ouyang, Y. Bi, N. Umezawa, M. Oshikiri, J. Ye, Nanophotocatalytic materials: possibilities and challenges. Adv. Mater. **24**, 229–251 (2012)

5. C.C. Chen, W.H. Ma, J.C. Zhao, Semiconductor-mediated photodegradation of pollutants under visible-light irradiation. Chem. Soc. Rev. **39**, 4206–4219 (2010)

6. M.Y. Guo, M.K. Fung, F. Fang, X.Y. Chen, A.M.C. Ng, A.B. Djurisic, W.K. Chan, ZnO and TiO_2 1D nanostructures for photocatalytic applications. J. Alloys Compd. **509**, 1328–1332 (2011)

7. M. Nolan, A. Iwaszuk, A.K. Lucid, J.J. Carey, M. Fronzi, Design of novel visible light active photocatalyst materials: surface modified TiO_2. Adv. Mater. **28**, 5425–5446 (2016)

8. J. Zhang, Y.P. Zhang, Y.K. Lei, C.X. Pan, Photocatalytic and degradation mechanisms of anatase TiO_2: a HRTEM study. Catal. Sci. Technol. **1**, 273–278 (2011)

9. C. Pan, Y. Zhu, New type of $BiPO_4$ oxy-acid salt photocatalyst with high photocatalytic activity on degradation of dye. Environ. Sci. Technol. **44**, 5570–5575 (2010)

10. S.U. Khan, M. Al-Shahry, Efficient photochemical water splitting by a chemically modified n-TiO_2. J. Sci. **297**, 2243–2245 (2002)

11. Z.G. Zou, J.H. Ye, K. Sayama, H. Arakawa, Direct splitting of water under visible light irradiation with an oxide semiconductor photocatalyst. Nature **414**, 625–627 (2001)

12. J. Jiang, X. Zhang, P.B. Sun, L.Z. Zhang, ZnO/BiOI heterostructures: photoinduced charge-transfer property and enhanced visible-light photocatalytic activity. J. Phys. Chem. **115**, 20555–20564 (2011)

13. S.S. Qian, C.S. Wang, W.J. Liu, Y.H. Zhu, W.J. Yao, X.H. Lu, An enhanced CdS/TiO_2 photocatalyst with high stability and activity: effect of mesoporous substrate and bifunctional linking molecule. J. Mater. Chem. **21**, 4945–4952 (2011)

14. H. Lin, H. Ye, B. Xu, J. Cao, S. Chen, Ag_3PO_4 quantum dot sensitized $BiPO_4$: a novel p–n junction Ag_3PO_4/$BiPO_4$ with enhanced visible-light photocatalytic activity. Catal. Commun. **37**, 55–59 (2013)

15. F.F. Duo, Y.W. Wang, X.M. Mao, X.C. Zhang, Y.F. Wang, C.M. Fan, A $BiPO_4$/BiOCl heterojunction photocatalyst with enhanced electron-hole separation and excellent photocatalytic performance. Appl. Surf. Sci. **340**, 35–42 (2015)

16. M. Lu, G. Yuan, Z. Wang, Y. Wang, J. Guo, Synthesis of $BiPO_4$/Bi_2S_3 heterojunction with enhanced photocatalytic activity under visible-light irradiation. Nanoscale Res. Lett. **10**, 385–391 (2015)

17. J. Kang, Q. Kuang, Z.X. Xie, L.S. Zheng, Fabrication of the SnO_2/α-Fe_2O_3 hierarchical heterostructure and its enhanced photocatalytic property. J. Phys. Chem. C **115**, 7874–7879 (2011)

18. A.Y. Murugan, T. Muraliganth, A. Manthiram, Rapid, facile microwave-solvothermal synthesis of graphene nanosheets and their polyaniline nanocomposites for energy strorage. Chem. Mater. **21**, 5004–5006 (2009)

19. Y.Q. Cong, Z. Li, Y. Zhang, Q. Wang, Q. Xu, Synthesis of α-Fe_2O_3/TiO_2 nanotube arrays for photoelectro-Fenton degradation of phenol. Chem. Eng. J. **191**, 356–363 (2012)

20. W. Yan, H.Q. Fan, C. Yang, Ultra-fast synthesis and enhanced photocatalytic properties of alpha-Fe_2O_3/ZnO core-shell structure. Mater. Lett. **65**, 1595–1597 (2011)

21. X.W. Zhang, M.H. Zhou, L.C. Lei, Co-deposition of photocatalytic Fe doped TiO_2 coatings by MOCVD. Catal. Commun. **7**, 427–431 (2006)

22. Y. Guo, G. Zhang, J. Liu, Y. Zhang, Hierarchically structured a-Fe_2O_3/Bi_2WO_6 composite for photocatalytic degradation of organic contaminants under visible light irradiation. RSC. Adv. **3**, 2963–2970 (2013)

23. N. Li, X. Hua, K. Wang, Y. Jin, J. Xu, M. Chen, F. Teng, In situ synthesis of uniform Fe_2O_3/BiOCl p/n heterojunctions and improved photodegradation properties for mixture dyes. Dalton Trans. **43**, 13742–13750 (2014)

24. S. Dutta, A.K. Patra, S. De, A. Bhaumik, B. Saha, Self-assembled TiO_2 nanospheres by using a biopolymer as a template and its optoelectronic application. ACS Appl. Mater. Interfaces **4**, 1560–1564 (2012)

25. M.H. Farzana, S. Meenakshi, Photo-decolorization and detoxification of toxic dyes using titanium dioxide impregnated chitosan beads. Int. J. Biol. Macromol. **70**, 420–426 (2014)

26. S. De, S. Dutta, A.K. Patra, B.S. Rana, A.K. Sinha, B. Saha, A. Bhaumik, General biopolymer templated porous TiO_2: an efficient catalyst for the conversion of unutilized sugars derived from hemicelluloses. Appl. Catal. A **435–443**, 197–203 (2012)

27. S. Thakur, S. Pandey, O.A. Arotiba, Development of a sodium alginate-based organic/inorganic superabsorbent composite hydrogel for adsorption of methylene blue. Carbohydr. Polym. **153**, 34–46 (2016)

28. M. Kimling, R.A. Caruso, Sol-gel synthesis of hierarchically porous TiO_2 beads using calcium alginate beads as sacrificial templates. J. Mater. Chem. **22**, 4073–4082 (2012)

29. M. Buaki-sogo, M. Serra, A. Primo, M. Alvaro, Alginate as template in the preparation of active titania photocatalysts. ChemCatChem **5**, 513–518 (2013)

30. C. Yu, X. Li, Z. Liu, X. Yang, Y. Huang, J. Lin, J. Zhang, C. Tang, Synthesis of hierarchically porous TiO_2 nanomaterials using alginate as soft templates. Mater. Res. Bull. **83**, 609–614 (2016)

31. J.Q. Albarelli, D.T. Santos, S. Murphy, M. Oelgemo, Use of Ca-alginate as a novelsupport for TiO_2 immobilization in methylene blue decolorisation. Water Sci. Technol. **60**, 1081–1087 (2009)

32. P. Cai, S. Zhou, D. Ma, S. Liu, W. Chen, S. Huang, Fe_2O_3-modified porous $BiVO_4$ nanoplates with enhanced photocatalytic activity. Nano-Micro Lett. **7**, 183–193 (2015)

33. Y. Zhang, B. Shen, H. Huang, Y. He, B. Fei, F. Lv, $BiPO_4$/reducedgraphene oxide composites photocatalyst with high photocatalytic activity. Appl. Surf. Sci. **319**, 272–277 (2014)

34. B. Qu, Y.Sun,L. Liu, C. Li, C. Yu, X. Zhang, Y. Chen, Ultrasmall Fe_2O_3 nanoparticles/MoS_2 nanosheets composite as high-performance anode material for lithium ion batteries. Sci. Rep. **7**, 42772 (2017). https://doi.org/10.1038/srep42772

35. T. Yamashita, P. Hayes, Analysis of XPS spectra of Fe^{2+} and Fe^{3+} ions in oxide materials. Appl. Surf. Sci. **254**, 2441–2449 (2008)

36. X.L. Hu, J.C. Yu, J.M. Gong, Q. Li, G.S. Li, Alpha-Fe_2O_3 nanorings prepared by a microwave-assisted hydrothermal process and their sensing properties. Adv. Mater. **19**, 2324–2329 (2007)

37. M. Hermanek, R. Zboril, I. Medrik, J. Pechousek, C. Gregor, Catalytic efficiency of iron(III) oxides in decomposition of hydrogen peroxide: competition between the surface area and crystallinity of nanoparticles. J. Am. Chem. Soc. **129**, 10929–10936 (2007)

38. V. Stengl, S. Bakardjieva, Molybdenum-doped anatase and its extraordinary photocatalytic activity in the degradation of orange

II in the UV and Vis regions. J. Phys. Chem. C **114**, 19308–19317 (2010)

39. T.J. Cai, M. Yue, X.W. Wang, Q. Deng, Preparation, characterization, and photocatalytic performance of $NdPW_{12}O_{40}/TiO_2$ composite catalyst. Chin. J. Catal. **28**, 10–16 (2007)

40. J.V. Kumar, R. Karthik, S.M. Chen, V. Muthuraj, K. Chelladurai, Fabrication of potato-like silver molybdate microstructures for photocatalytic degradation of chronic toxicity ciprofloxacin and highly selective electrochemical detection of H_2O_2. Sci. Rep. **6**, 1–13 (2016)